ACS Energy Letters

http://pubs.acs.org/journal/aelccp



# Sodium−Sulfur Batteries Enabled by a Protected Inorganic/Organic Hybrid Solid Electrolyte

Yuxun Ren, Nicholas Hortance, JamesR. McBride, and Kelsey B. Hatzell*

Cite This: *ACS Energy Lett.* 2021, 6, 345−353

Read Online

ACCESS | Metrics & More | Article Recommendations | Supporting Information

**ABSTRACT:** **Sodium−sulfur batteries are promising energy-dense, cost-effective energy storage systems. However, a low-resistance solid electrolyte is necessary to stabilize the sodium anode. While sulfide-based solid electrolytes offer high ionic conductivity, they suffer from chemical reactivity when in contact with sodium metal and are mechanically brittle. This paper implements an *in situ* cross-linking reaction to embed sodium-ion-conducting sodium thioantimonate in a protective polymer host. The enhanced flexibility enables the formation of a thin but transferable hybrid electrolyte film (30 μm in thickness, 65 ohm cm$^2$ room temperature resistance). Owing to the chemical bonding between sodium thioantimonate and the polymer, the hybrid electrolyte maintains a stable interface with sodium when cycling at a current density of 0.5 mA cm$^{-2}$. The hybrid solid electrolyte protects the sodium metal from corroding with polysulfide-containing liquid electrolyte and enables the stable operation of a sodium−sulfur battery using a nonencapsulated sulfur cathode for 90 cycles.**

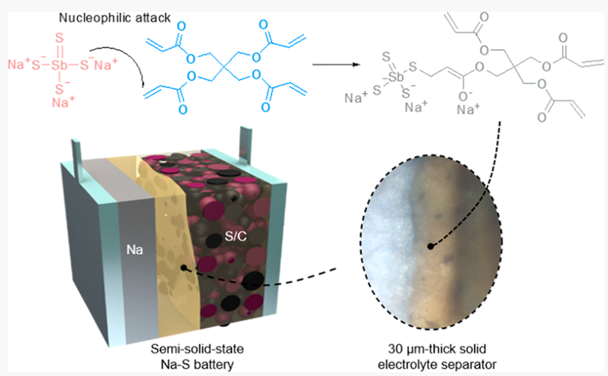


Sodium−sulfur (Na−S) batteries are an energy-dense (1580 Wh L$^{-1}$ theoretical energy density) and cost-effective (\$300−500 kWh$^{-1}$) option for grid-scale energy storage.[1−4] Commercialized high-temperature Na−S batteries usually require an operating temperature above 300 °C with sodium and sulfur in their molten states.[5] Lowering the operating temperature can potentially extend their applications to electric vehicles, portable electronics, and stationary storage applications.[6−14] Typically, low-temperature Na−S batteries employ liquid binary electrolytes. During discharge, sulfur is reduced in a multistep process to solvated sodium polysulfides (NaPS) and insoluble $Na_2S_2$/$Na_2S$.[15] While the solvation of NaPS intermediates improves the reaction kinetics, NaPS intermediates can transport from the cathode to the anode (crossover), which limits the overall cell performance. The sodium anode can reduce the NaPS to create insoluble byproducts ($Na_2S_2$/$Na_2S$), which leads to irreversible capacity decay. In addition, during charge, irregular electrodeposition can be amplified at high charge rates because of the formation of concentration gradients.[3,16,17] This can lead to the formation of high-surface-area sodium deposits (mossy and dendrite), which accelerate side reactions, consume active sodium, and can potentially short the cell.[18−20]

Single-ion-conducting solid electrolytes can mitigate the presence of a $Na^+$ concentration gradient, regularize sodium electrodeposition and dissolution mechanisms, and suppress NaPS crossover.[21−26] Ideal solid electrolytes fulfill the requirements of low resistance, high mechanical ductility, and chemical stability. Inorganic-oxide-based solid electrolytes ($\beta$-$Al_2O_3$) are typically used in high-temperature Na−S battery systems.[27] However, processing thin oxides at scale remains a considerable challenge due to the high sintering temperature and low mechanical strength of oxides. Sulfide solid electrolytes are more ductile and processable.[28−30] Unfortunately, most of the reported sulfide solid electrolytes (e.g., $Na_3PS_4$, $Na_3P_{1-x}As_xS_4$, $Na_3SbS_4$) react with the sodium metal. Reacting elements (P, As, or Sb) in the sulfide solid electrolytes can create an electronically conducting interphase that impacts transport and parastic sodium deposition.[3132] To mitigate a decomposition effect, a range of protection approaches are

**Received:** December 1, 2020
**Accepted:** December 21, 2020
**Published:** December 31, 2020







https://dx.doi.org/10.1021/acsenergylett.0c02494
*ACS Energy Lett.* 2021, 6, 345−353

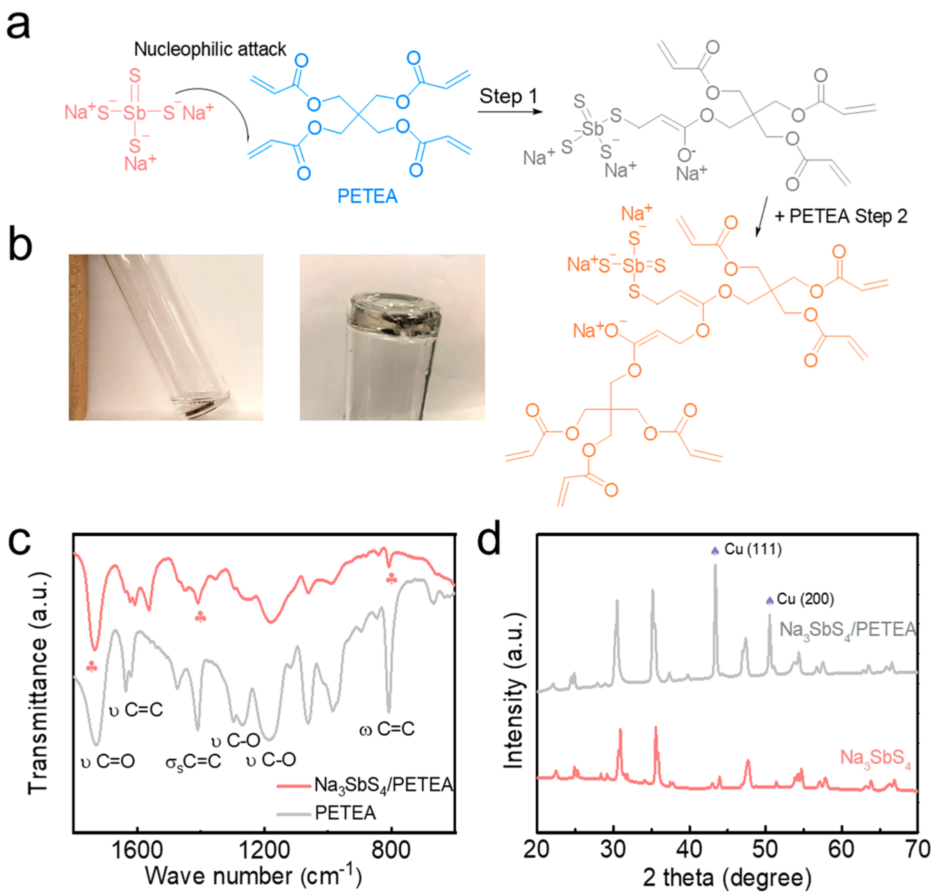


**Figure 1. Cross-linking sulfide with polymer. (a) Schematic showing the cross-linking of PETEA initiated by $Na_3SbS_4$. Step 1 shows the addition of PETEA to $Na_3SbS_4$. Step 2 shows the continuous addition of PETEA caused by the reaction between the enol oxygen anion and terminal C=C bond of PETEA. (b) Optical photo showing the cross-linking of PETEA initiated by a $Na_3SbS_4$ pellet (left: PETEA monomer was flowable before cross-linking; right: PETEA cross-linked with $Na_3SbS_4$ and became a solid gel. (c) FTIR of the $Na_3SbS_4$/PETEA hybrid and PETEA monomer. (d) XRD of the $Na_3SbS_4$/PETEA hybrid (casted on a Cu foil) and a $Na_3SbS_4$ pellet.**

often implemented. Recent studies on $Na_3SbS_4$ reveal that a hybrid sulfide solid surface with a polymer or surface modification of solid electrolytes can increase the energy barrier of decomposition. Polymer electrolytes, for example, those containing poly(ethylene oxide) and sodium salts, can block electron transport and suppress the direct reduction of $Na_3SbS_4$ by sodium.[29,3334] However, previous studies reported continuous side reactions between polymer melts and sulfide solid electrolytes.[35] Reacting $Na_3SbS_4$ with a stabilizing agent, for example, water, results in a wider electrochemical window for this type of solid electrolyte due to the formation of a passivating phase ($Na_3SbS_4 \cdot 8H_2O$).[36] However, the *in situ* reaction on the $Na_3SbS_4$ surface is challenging to control and might lead to the formation of the much less conductive $Na_3SbS_4 \cdot 9H_2O$ phase.

Here, we design an *in situ* cross-linking reaction to combine $Na^+$-conducting sodium thioantimonate ($Na_3SbS_4$) electrolyte with a flexible gel polymer. The hybrid solid electrolyte demonstrates higher chemical stability and mechanical durability than the purely inorganic solid electrolyte. We reveal that $Na_3SbS_4$ can initiate the cross-linking of liquid pentaerythritol tetraacrylate (PETEA) monomer. The cross-linking approach enables scalable production of a thin (≤30 $\mu$m), transferable hybrid electrolyte film. Meanwhile, the cross-linking reaction improves the stability of $Na_3SbS_4$ and suppresses its dissolution in liquid electrolyte. The sodium anode protected with the hybrid solid electrolyte can enable the stable operation of a Na−S battery with a sulfur loading of 1.0 mg $cm^2$ for 90 cycles.

The hybrid $Na^+$-conducting solid electrolyte combines an inorganic sulfide solid electrolyte and a cross-linkable monomer. Sodium thioantimonate ($Na_3SbS_4$) was chosen as the inorganic solid electrolyte, because it displays good transport properties with an ionic conductivity nearing $10^{-4}$–$10^{-3}$ S $cm^{-1}$ at room temperature. Furthermore, sodium thioantimonate can be synthesized and processed through facile, solution-based approaches.[23,37] However, sodium thioantimonate is not chemically stable and is prone to dissolution and decomposition when in contact with liquid electrolyte and sodium metal. The chemical stability of $Na_3SbS_4$ was improved by incorporation of a gel polymer, which served as a protective barrier toward spontaneous decomposition when in contact with sodium metal. Herein, we explored pathways to cross-link PETEA directly to the inorganic solid electrolyte (Figure 1a).[38] $Na_3SbS_4$ and PETEA will spontaneously cross-link at elevated temperatures between 120 and 150 °C, based on the classical thiol−ene Michael addition mechanism.[39−42] The reaction mechanism (Figure 1a) reported here is similar to the traditional base-catalyzed Michael addition with a few noticeable differences.[43] First, a sodium salt serves as a direct sulfur source, which alleviates the need for a Lewis base catalyst to dissociate $H^+$


https://dx.doi.org/10.1021/acsenergylett.0c02494
ACS Energy Lett. 2021, 6, 345−353

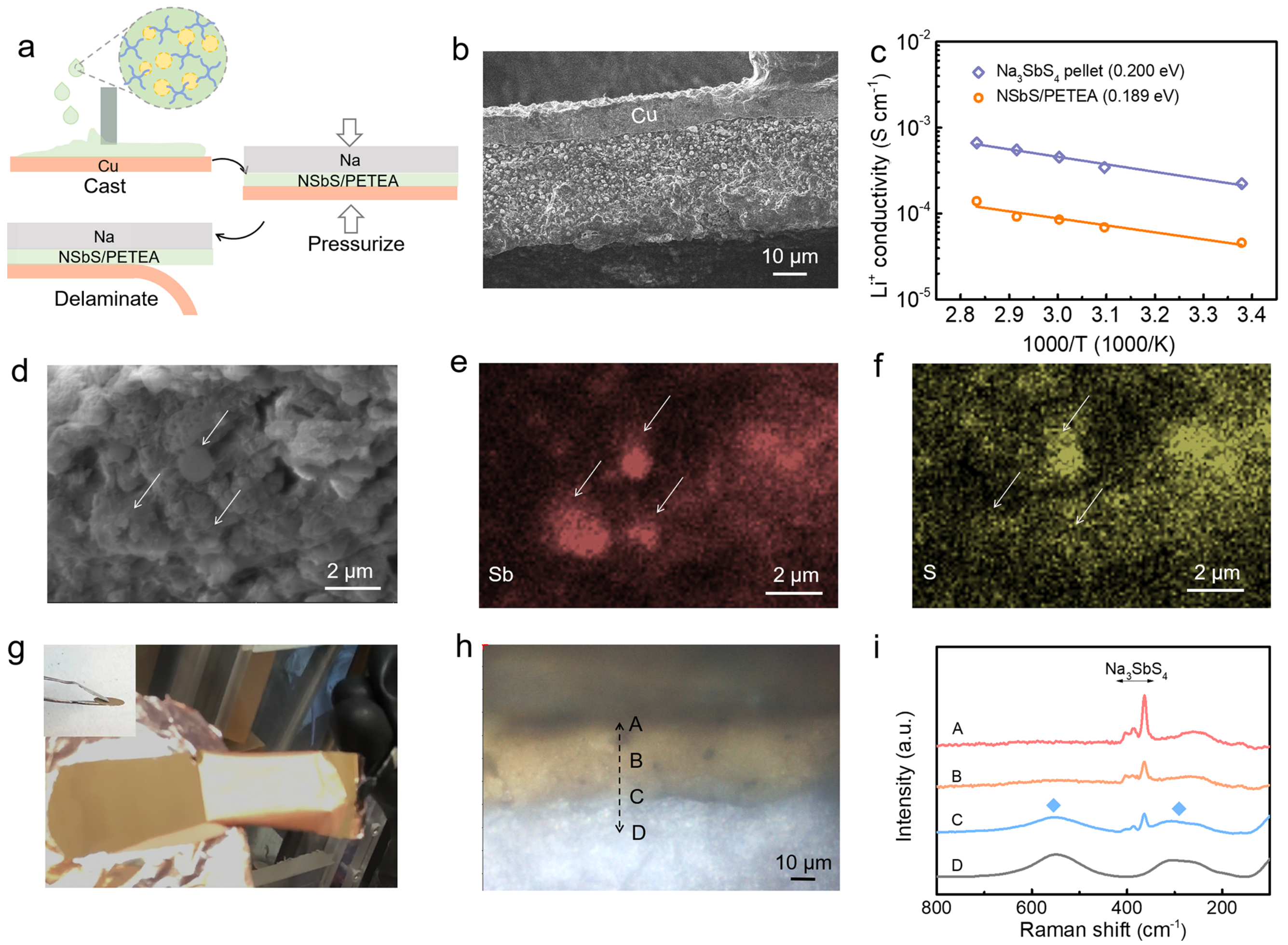


**Figure 2. Protecting sodium with a sulfide/polymer hybrid electrolyte film. (a) Fabrication of $Na_3SbS_4$/PETEA−Na, involving blade-casting and transfer-printing. (b) SEM image of the cross section of $Na_3SbS_4$/PETEA−Cu. (c) Arrhenius plot of the ionic conductivity measured from the $Na_3SbS_4$/PETEA hybrid electrolyte and the $Na_3SbS_4$ solid electrolyte pellet. (d−f) SEM/EDS mapping results of $Na_3SbS_4$/PETEA. (g) Optical photo of $Na_3SbS_4$/PETEA−Na with the Cu substrate being peeled off. (h,i) Optical image of the cross section of $Na_3SbS_4$/PETEA−Na (h), and corresponding Raman spectra (i). The marked spots (from A to D) were measured using Raman spectroscopy (1 μm spatial resolution). The peaks marked by diamonds in the Raman spectra come from the sodium metal.**

from the thiol (R−SH) during the addition reaction. Second, the reaction progresses in a quasi-solid environment, because the PETEA feedstock exists in liquid form. The reaction can be observed by submersing a $Na_3SbS_4$ pellet directly into the liquid PETEA at 150 °C (Figure 1b). Under these conditions, $Na_3SbS_4$ and liquid PETEA cross-link and form a solid gel. The Lewis basic $SbS_4^{3-}$ unit can initiate nucleophilic attack toward the terminal C=C bond in PETEA (Figure 1a). This step links $Na_3SbS_4$ with PETEA and converts the oxygen double bond into Lewis basic oxonium ions. Oxonium ions will continue to react with the PETEA monomer and create a gel network. After the cross-linking reaction, there was a visible intensity decrease for the vinyl groups at 1308 $cm^{-1}$ (C=C scissoring) and 708 $cm^{-1}$ (C=C out of plane deformation) in the FTIR spectra. This suggests that the terminal C=C bonds on the PETEA reacted (Figure 1c).[38] FTIR spectra on different hybrid electrolytes ($Na_3SbS_4$/PETEA) with varying quantities of PETEA were studied to better understand the reaction mechanism (Figure S1). Hybrid electrolytes with less PETEA demonstrate less unreacted PETEA arms. A decrease in the C=O peak intensity around 1750 $cm^{-1}$ was observed. This is likely because the C=O bond is converted to C−O−$Na^+$. The latter product could be further converted to C−O−C after reacting with the C=C bond. In contrast, the peak intensity of the C−O vibration at 1184 $cm^{-1}$ maintained a relatively high value. Since the reaction only takes place at the surface of $Na_3SbS_4$, the bulk structure of $Na_3SbS_4$ remained unchanged (Figures 1d and S2).

The hybrid-electrolyte-protected sodium foil ($Na_3SbS_4$/PETEA−Na) was processed using a facile two-step approach. First, the electrolyte was cast onto a foil. In a subsequent step, the barrier film was transferred directly to the sodium electrode (Figure 2a). Blade-coated hybrid electrolytes ($Na_3SbS_4$/PETEA) were approximately 30 μm in thickness (Figure 2b). Scanning electron microscopy demonstrates that the inorganic particles are uniformly distributed within the polymer matrix. The inorganic $Na_3SbS_4$ particles vary in size but all exceed 500 nm (Figures S3 and S4). $Na^+$ ions can transport across the connected $Na_3SbS_4$ network in the hybrid electrolyte. The 30-μm-thick hybrid electrolyte exhibited an areal resistance of 65 ohm $cm^2$ and an ionic conductivity of 0.047 mS $cm^{-1}$ at room temperature (more details can be found in Figure S5). This is equivalent to 22% of the ionic conductivity of the all-inorganic $Na_3SbS_4$ electrolyte (0.22 mS


https://dx.doi.org/10.1021/acsenergylett.0c02494
ACS Energy Lett. 2021, 6, 345−353

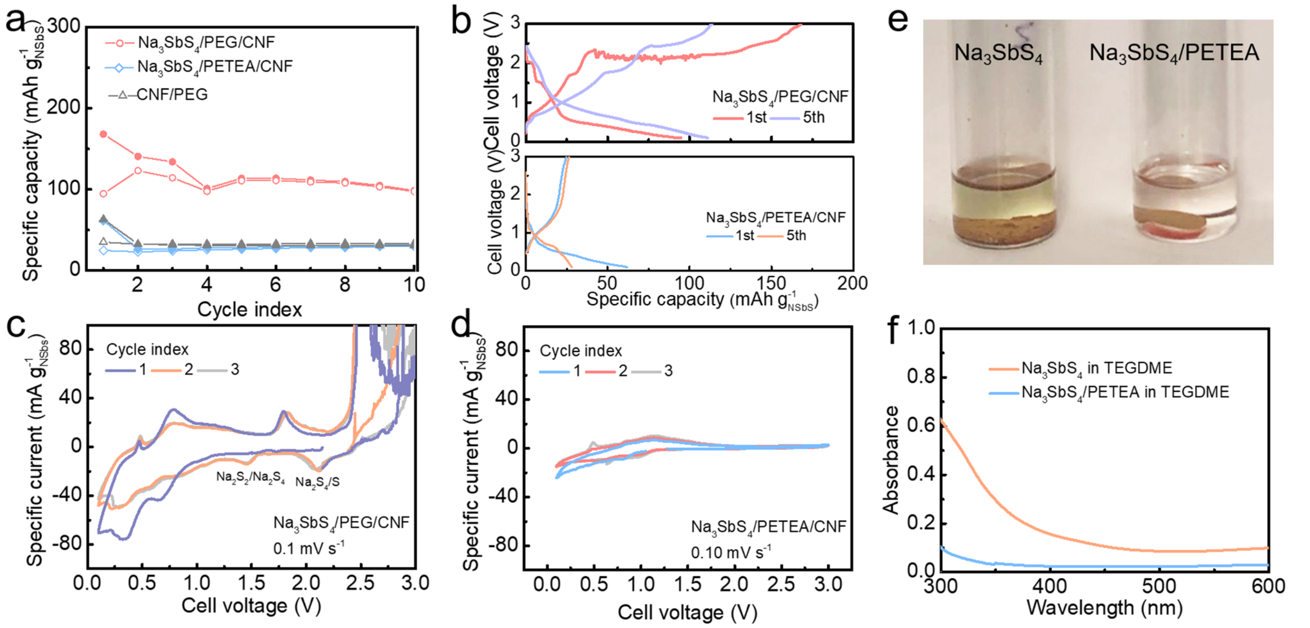


**Figure 3. (a) Cyclability of the Na|$Na_3SbS_4$ half cells with different binders (PEG and PETEA). (b) Corresponding voltage profiles of the half cells. (c,d) Cyclic voltammetry profile for the half cells. (e) Soaking of $Na_3SbS_4$ and $Na_3SbS_4$/PETEA−Cu in liquid electrolyte solvent. (f) UV−vis of the solvents after soaking.**

$cm^{-1}$) (Figure 2c). The $Na_3SbS_4$ particles are well distributed within the polymer matrix and form interconnected pathways for continuous ion transport. Energy dispersive spectroscopy further confirms the connected nature of the inorganic solid electrolyte particles (Figures 2d−f and S4). The ionic conductivity can be improved either through microstructure control[19,28,29] or using a higher ionic conductivity inorganic material, e.g., the recently discovered $Na_3Sb_{1-x}W_xS_4$.[37,44,45] However, this is outside the scope of this study. Compared with reported methods in literature, the processing approach described here avoids the use of solvents and enables adequate adhesion between sulfide and polymer constituents (a detailed comparison can be found in Table S1).[46−49] Furthermore, the approach is compatible with scalable blade-casting processes that already exist in battery manufacturing plants.

The hybrid solid electrolyte was transferred from the copper foil to the sodium anode in a secondary process using a transfer-printing approach (Figure 2g). All-inorganic $Na_3SbS_4$ tends to react with sodium metal. Furthermore, all-inorganic $Na_3SbS_4$ does not wet sodium metal well, which leads to nonuniform contact and irregular, nonuniform ionic flux. In contrast, the oxygen-rich functional groups in the hybrid solid electrolyte exhibit a strong adhesion with the sodium metal, which enables good, continuous contact. After a moderate pressure is applied, the hybrid electrolyte can strongly adhere on the sodium metal surface (Figure 2g).[33] There also exists a strong adhesion between the solid electrolyte particles and polymer matrix due to the covalent bonding, which guarantees the mechanical integrity of the hybrid electrolyte during the transfer-printing process (Figure 2g). Optical microscopy and Raman spectroscopy confirm the intimate contact between sodium and the hybrid electrolyte. In the Raman spectra, the peaks representing $Na_3SbS_4$ and sodium coexist at the interface region (spot C) (Figure 2h,i).

$Na_3SbS_4$ exhibits a narrow voltage window (1.55−2.3 V vs $Na/Na^+$) and is soluble in many electrolyte solvents.[36] To examine the practical stability of $Na_3SbS_4$ in batteries, we fabricated a $Na_3SbS_4$ working electrode (cathode) using $Na_3SbS_4$ as the active material, polyethlyene glycol (PEG, MW = 1000) as the binder, and carbon nanofiber (CNF) as the conductive additive. Liquid electrolyte was also added to fully wet the electrode. The Na|$Na_3SbS_4$ half cell achieved an initial discharge capacity of 95 $mAhg^{-1}_{NSbS}$ and constantly maintained above 100 $mAhg^{-1}_{NSbS}$ (theoretical capacity 672 $mAhg^{-1}_{NSbS}$) (Figure 3a). During initial discharge, sodiation of $Na_3SbS_4$ created $Sb/Na_2S$ in the first stage (2.3−0.6 V vs $Na/Na^+$), and Sb alloyed with sodium to form $Na_3Sb$ in the second stage (0.6−0.01 V vs $Na/Na^+$).[50] During charge, $Na_2S$ and $Na_3Sb$ were oxidized to $Sb_2S_5$ and sulfur. There was formation of NaPS intermediates during charge, leading to the NaPS crossover and charging voltage profile fluctuation (Figure 3b).[5136] Cyclic voltammetry (Figure 3c) clearly distinguishes the reduction peaks for sulfur redox reactions (2.12 and 1.47 V), conversion from $Sb_2S_5$ to $Sb/Na_2S$ (0.58 V), and the alloying of Sb (0.35 V). After the first three cycles, the active sulfur species diffused to the sodium anode side and were irreversibly consumed. In the following cycles (4−10 cycles), the residual $Sb_2S_5$ in the cathode reversibly uptook/released sodium ($Sb_2S_5$ + $16Na^+$ + $16e^{-}2Na_3Sb$ + $5Na_2S$) without creating NaPS intermediates (Figure 3b), leading to a relatively stable capacity.[50]

Cross-linking with PETEA induces a higher energy barrier for sodiation-induced decomposition. Also, the polymer insulates against electron transport, which propagates decomposition.[33] When PETEA is replaced with a non-ion-conducting polymer (PEG binder), a decrease in the initial capacity was observed (62 mAh $g^{-1}_{NSbS}$). A reversible capacity around 30 mAh $g^{-1}_{NSbS}$ was observed with PEG over several cycles (Figure 3a). The charge/discharge (Figure 3b) and cyclic voltammetry (Figure 3d) behavior was similar to the blank electrode (fabricated with only CNF and PEG) (Figure S5). The capacity mainly originated from the intercalation of $Na^+$ into the graphitized CNF, rather than the decomposition of $Na_3SbS_4$.[52] The good electrochemical stability enables the


https://dx.doi.org/10.1021/acsenergylett.0c02494
ACS Energy Lett. 2021, 6, 345−353

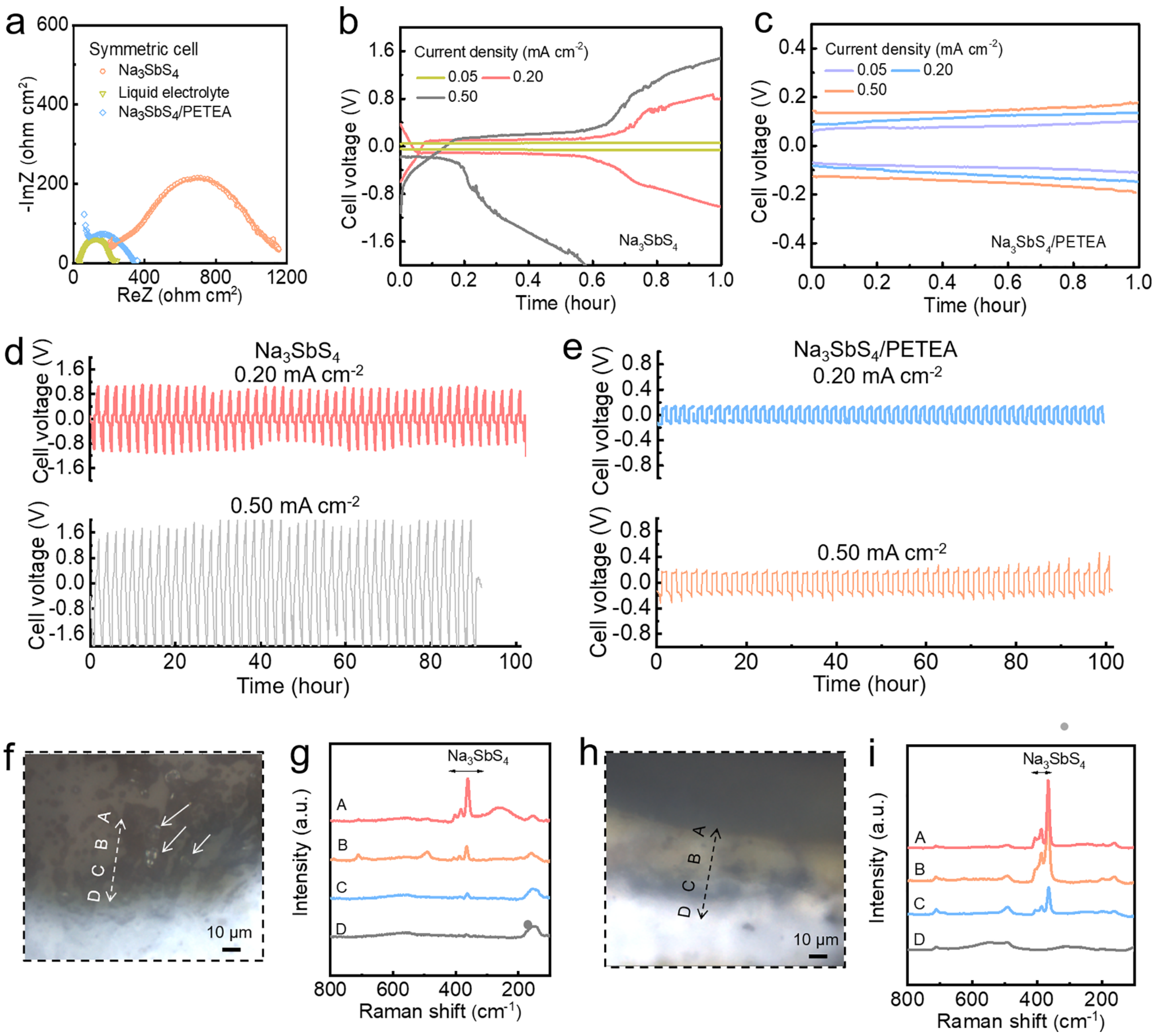


**Figure 4. Symmetric Na|Na cell test. (a) EIS profiles of the symmetric cells using different electrolytes (liquid electrolyte, $Na_3SbS_4$, and $Na_3SbS_4$/PETEA). (b,c) Voltage profiles of symmetric cells using $Na_3SbS_4$ solid electrolyte (b) and $Na_3SbS_4$/PETEA hybrid electrolyte (c). (d,e) Cyclability of symmetric cell using $Na_3SbS_4$ solid electrolyte (d) and $Na_3SbS_4$/PETEA hybrid electrolyte (e). (f,g) Optical image of cycled Na|$Na_3SbS_4$ interface (f) and the Raman spectra (g). The Na deposits inside the $Na_3SbS_4$ are marked by arrows. (h,i) Optical image of the cycled Na|$Na_3SbS_4$/PETEA interface (h) and the Raman spectra (i). The marked symbols (from A to D) were measured by Raman spectroscopy. In the Raman spectra, the peak marked by a dot comes from the $Na_xSb$ alloy.**

wide application of the hybrid electrolyte in both the cathode and anode.

In addition, $Na_3SbS_4$ is observed to readily dissolve in tetraglyme (Figure 3e). The electron-rich oxygen from the solvent molecule exacerbates electrostatic interactions between the $Na^+$ cation from $Na_3SbS_4$, resulting in the dissolution of the solid electrolyte.[53] In contrast, the polymer in the hybrid electrolyte is soluble and anchors the $Na_3SbS_4$ with covalent bonds. This results in the suppressed dissolution of $Na_3SbS_4$, as can be confirmed from the UV–vis spectra (Figure 3e,f).

The high stability of $Na_3SbS_4$/PETEA enables its use as the anode protective layer. We assembled a symmetric cell for the evaluation of the resistances and cycling performance using different electrolytes ($Na_3SbS_4$ solid electrolyte, $Na_3SbS_4$/PETEA hybrid electrolyte, and $NaClO_4$/tetraglyme-based liquid electrolyte). With the use of a 700-$\mu$m-thick solid electrolyte, the overall resistance was around 1150 $\Omega$ cm$^{-2}$, with 540 $\Omega$ cm$^{-2}$ of resistance coming from the interface (Figure 4a, fitting result can be found in Figure S7). With the use of the 60-$\mu$m-thick $Na_3SbS_4$/PETEA hybrid electrolyte, the symmetric cell exhibited a reasonable overall resistance of 340 $\Omega$ cm$^{-2}$. In comparison, the symmetric cell using a liquid electrolyte and a 25-$\mu$m-thick porous separator exhibits an overall resistance of around 230 $\Omega$ cm$^2$. Thus, the hybrid electrolyte and liquid electrolyte exhibited a similar combined interfacial and charge transfer resistances around 730 $\Omega$ cm$^2$ (Figure S7). The low resistance observed suggests that the hybrid electrolyte is a promising approach to protect sodium metal anodes.

The all-inorganic $Na_3SbS_4$ solid electrolyte pellet demonstrates significant increases in the cell polarization during symmetric cell cycling experiments at 0.2 or 0.5 mA cm$^{-2}$ (1 h charge/discharge for each cycle, Figure 4b,d). The chemical/electrochemical reduction of $Na_3SbS_4$ at the sodium surface


https://dx.doi.org/10.1021/acsenergylett.0c02494
ACS Energy Lett. 2021, 6, 345−353

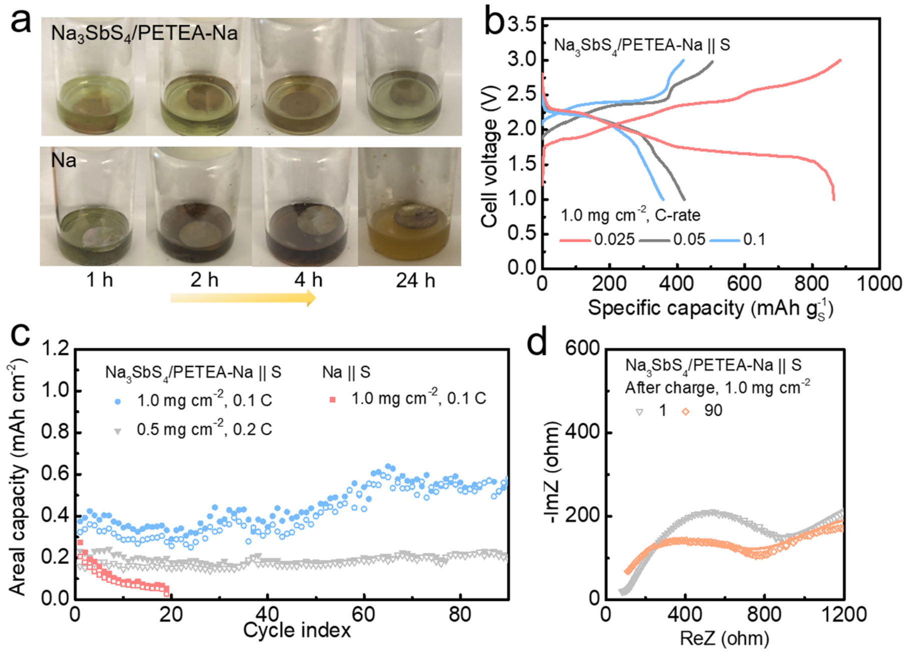


**Figure 5. Sodium−sulfur battery tests. (a) Soaking of $Na_3SbS_4$/PETEA−Na and bare Na in the liquid electrolyte containing sulfur powder. (b) Voltage profiles of a Na−S battery with a sulfur loading of 1.0 mg $cm^{-2}$. (c) Cycling performance with a sulfur loading of 0.5 or 1.0 mg $cm^{-2}$. (d) Corresponding EIS profiles over cycling.**

creates an interphase region composed of $Na_3Sb/Na_2S$ products (Figure 4f,g).[50,54] $Na_xSb$ is electronically conductive, which can lead to the uncontrollable growth of the interphase region. Uncontrolled interphase growth led to cell shorting after 45 cycles at 0.5 mA $cm^{-2}$. Symmetric cells using a liquid electrolyte demonstrated increases in the overpotential during cycling due to surface passivation, irregular sodium deposition, and showed a voltage spike after 40 cycles (Figure S7).[55,56]

In contrast, the hybrid solid electrolyte cycled over 50 times (100 h) at 0.2 and 0.5 mA $cm^{-2}$ and demonstrated a relatively flat voltage profile (Figure 4c,e). Hybrid solid electrolytes were cycled with and without a liquid electrolyte. The liquid electrolyte was used primarily to achieve intimate contact between the two hybrid electrolytes as detailed in the experimental section. However, electrolytes can operate without liquid if an applied pressure is utilized. Performance was similar for both cases (Figure S9). The critical current density of the symmetric cell using the hybrid electrolyte was 0.55 mA $cm^{-2}$ (Figure S10). A large voltage increase was observed when cycling above the critical current density, which is likely due to the delamination of sodium from the hybrid electrolyte. After cycling, the interface between hybrid electrolyte and sodium metal maintained an intimate contact over cycling with minor signs of side products (Figures 4h,i and S10). The Na-metal−$Na_3SbS_4$ contact area is greatly diminished in the hybrid form. However, some of $Na_3SbS_4$ will undoubtedly react with the sodium metal. This can lead to the formation of an interphase region, which is composed of $Na_3Sb/Na_2S$ as shown in Figure S12. Sodium ions can transport from the $Na_3SbS_4$ to the mixed conductive interphase and deposit at the sodium metal electrode. The addition of PETEA prevents the continuous growth of a mixed conductive layer, as $Na_3SbS_4$/PETEA is more electrochemically stable. Compared with literature using sulfide- or selenide-based solid electrolytes, our work achieved a relatively high areal capacity and a low resistance, without the use of any anode/electrolyte interlayer (Table S2).[33,36,57−59]

The hybrid electrolyte acts as an effective barrier between sodium metal and soluble NaPS in the sulfur cathode, which is critical for enabling Na−S batteries. To confirm this, we immersed the bare Na and $Na_3SbS_4$/PETEA−Na in the liquid electrolyte containing sulfur powder. Using the bare Na, the liquid electrolyte color turned to dark green and gray after resting for 4 h due to the formation of high-order NaPS ($Na_2S_6$, $Na_2S_8$). The high-order NaPS is reduced when in contact with Na metal for a long time and changes color (Figure 5a).[60] In contrast, there was no observable change in the hybrid electrolyte color when in contact with the sodium metal. The lack in color change indicates that the liquid electrolyte cannot penetrate through the hybrid solid electrolyte and react with the sodium metal (Figure S13).[61]

The protected sodium anode was studied in a full cell with a nonencapsulated sulfur/carbon nanofiber composite cathode in the batteries. At a sulfur loading of 1.0 mg $cm^{-2}$, the battery achieved around 360, 450, and 850 mAh $g_S^{-1}$ at 0.1, 0.5, and 0.25 C (Figure 5b). At a low current density (e.g., 0.25 C), two discharge plateaus were observed. The upper plateau represents the conversion from $S_8$ to $Na_2S_4$, and the lower plateau represents the conversion from $Na_2S_4$ to $Na_2S_2$.[51] At a high current density (e.g., 0.1 C), a single plateau was observed and is attributed to the $S_8/Na_2S_4$ redox reaction. To avoid the formation of insulating $Na_2S_2$ solid at the lower plateau, the voltage window was constrained, and cycling was run at 0.1 C (0.11 mA $cm^{-2}$).[51] The capacity (discharge) showed a gradual increase from 0.92 to 0.52 mAh $cm^{-2}$ during 90 cycles. This is hypothesized to be a result of changing interfacial area due to the potential pore formation and delamination (Figure 5c). Over cycling, the overall resistance at room temperature was maintained below 1000 ohm (Figures 5d and S14). At a smaller capacity around 0.2 mAh $cm^{-2}$ (sulfur loading 0.5 mg $cm^{-2}$, Figure S15) there was less capacity evolution during


https://dx.doi.org/10.1021/acsenergylett.0c02494
ACS Energy Lett. 2021, 6, 345−353

cycling. In comparison, the battery with a bare Na anode decayed to 27.5% at a sulfur loading of 1.0 mg $cm^{-2}$ merely after 15 cycles (Figure 5c). The sodium−sulfur battery performance can be further improved in future work via optimization of the cathode. Herein, we demonstrate a hybrid solid electrolyte that can effectively stabilize sodium anode at a higher temperature (e.g., 60 °C). The higher operating temperature boosts the specific capacity of the sulfur cathode (Figure S16). The performance of the cathode can be also improved through using advanced electrolytes and engineering of the cathode composition and microstructure.[51,62,63]

Herein, we implement an *in situ* cross-linking approach to achieve a hybrid sodium-ion-conducting solid electrolyte. The combination of a polymer and an inorganic material enables protection of both the inorganic and sodium metal and stable electrodeposition and dissolution reactions. The hybrid electrolyte decreases consumptive side reactions (NaPS) that typically occur at the anode interface and enable a long cycle life for the nonencapsulated sulfur cathode. The hybrid electrolyte can be generalized to other Na-based anodes, including porous sodium scaffolds and sodium alloys. The hybrid solid electrolyte provides a scalable pathway to integration of thin, flexible, and resilient solid electrolytes and are thus promising approaches for next generation low-cost sodium−sulfur batteries.

## ■ ASSOCIATED CONTENT

### Supporting Information

The Supporting Information is available free of charge at https://pubs.acs.org/doi/10.1021/acsenergylett.0c02494.

Experimental description and additional imaging (PDF)

## ■ AUTHOR INFORMATION


### Corresponding Author

**Kelsey B. Hatzell** − *Department of Mechanical Engineering, Vanderbilt University, Nashville, Tennessee 37235, United States; Chemical and Biomolecular Engineering, Vanderbilt University, Nashville, Tennessee 37235, United States;* orcid.org/0000-0002-5222-7288; Email: kelsey.b.hatzell@vanderbilt.edu

### Authors

**Yuxun Ren** − *Department of Mechanical Engineering, Vanderbilt University, Nashville, Tennessee 37235, United States*

**Nicholas Hortance** − *Interdisciplinary Material Science Program, Vanderbilt University, Nashville, Tennessee 37235, United States*

**JamesR. McBride** − *Department of Chemistry and The Vanderbilt Institute of Nanoscale Science and Engineering, Vanderbilt University, Nashville, Tennessee 37235, United States;* orcid.org/0000-0003-0161-7283

Complete contact information is available at: https://pubs.acs.org/10.1021/acsenergylett.0c02494


### Notes

The authors declare no competing financial interest.

## ■ ACKNOWLEDGMENTS

The authors were supported by the National Science Foundation under grant no. 1847029. The authors acknowledge the Vanderbilt Institute of Nanoscience and Engineering (VINSE) for access to their shared characterization facilities. K.B.H. acknowledges support from Toyota Research Institute in North America and the ECS/Toyota Young Investigator Fellowship.

## ■ REFERENCES


(1) Manthiram, A.; Yu, X. Ambient temperature sodium−sulfur batteries. *Small* **2015**, *11*, 2108−2114.

(2) Wang, Y.-X.; Zhang, B.; Lai, W.; Xu, Y.; Chou, S.-L.; Liu, H.-K.; Dou, S.-X. Room-temperature sodium-sulfur batteries: a comprehensive review on research progress and cell chemistry. *Adv. Energy Mater.* **2017**, *7*, 1602829.

(3) Lee, B.; Paek, E.; Mitlin, D.; Lee, S. W. Sodium metal anodes: Emerging solutions to dendrite growth. *Chem. Rev.* **2019**, *119*, 5416−5460.

(4) Wang, H.; Matios, E.; Luo, J.; Li, W. Combining theories and experiments to understand the sodium nucleation behavior towards safe sodium metal batteries. *Chem. Soc. Rev.* **2020**, *49*, 3783−3805.

(5) Hueso, K. B.; Armand, M.; Rojo, T. High temperature sodium batteries: status, challenges and future trends. *Energy Environ. Sci.* **2013**, *6*, 734−749.

(6) Carter, R.; Oakes, L.; Douglas, A.; Muralidharan, N.; Cohn, A. P.; Pint, C. L. A sugar-derived room-temperature sodium sulfur battery with long term cycling stability. *Nano Lett.* **2017**, *17*, 1863−1869.

(7) Wei, S.; Xu, S.; Agrawral, A.; Choudhury, S.; Lu, Y.; Tu, Z.; Ma, L.; Archer, L. A. A stable room-temperature sodium−sulfur battery. *Nat. Commun.* **2016**, *7*, 11722.

(8) Xu, X.; Zhou, D.; Qin, X.; Lin, K.; Kang, F.; Li, B.; Shanmukaraj, D.; Rojo, T.; Armand, M.; Wang, G. A room-temperature sodium−sulfur battery with high capacity and stable cycling performance. *Nat. Commun.* **2018**, *9*, 3870.

(9) Wang, Y.-X.; Yang, J.; Lai, W.; Chou, S.-L.; Gu, Q.-F.; Liu, H. K.; Zhao, D.; Dou, S. X. Achieving high-performance room-temperature sodium−sulfur batteries with S@ interconnected mesoporous carbon hollow nanospheres. *J. Am. Chem. Soc.* **2016**, *138*, 16576−16579.

(10) Kumar, D.; Rajouria, S. K.; Kuhar, S. B.; Kanchan, D. Progress and prospects of sodium-sulfur batteries: a review. *Solid State Ionics* **2017**, *312*, 8−16.

(11) Fan, L.; Ma, R.; Yang, Y.; Chen, S.; Lu, B. Covalent sulfur for advanced room temperature sodium-sulfur batteries. *Nano Energy* **2016**, *28*, 304−310.

(12) Wang, Y.-X.; Zhang, B.; Lai, W.; Xu, Y.; Chou, S.-L.; Liu, H.-K.; Dou, S.-X. Room-temperature sodium-sulfur batteries: a comprehensive review on research progress and cell chemistry. *Adv. Energy Mater.* **2017**, *7*, 1602829.

(13) Kohl, M.; Borrmann, F.; Althues, H.; Kaskel, S. Hard Carbon Anodes and Novel Electrolytes for Long-Cycle-Life Room Temperature Sodium-Sulfur Full Cell Batteries. *Adv. Energy Mater.* **2016**, *6*, 1502185.

(14) Matios, E.; Wang, H.; Wang, C.; Li, W. Enabling safe sodium metal batteries by solid electrolyte interphase engineering: a review. *Ind. Eng. Chem. Res.* **2019**, *58*, 9758−9780.

(15) Wenzel, S.; Metelmann, H.; Raiß, C.; Dürr, A. K.; Janek, J.; Adelhelm, P. Thermodynamics and cell chemistry of room temperature sodium/sulfur cells with liquid and liquid/solid electrolyte. *J. Power Sources* **2013**, *243*, 758−765.

(16) Dixit, M. B.; Singh, N.; Horwath, J. P.; Shevchenko, P. D.; Jones, M.; Stach, E. A.; Arthur, T. S.; Hatzell, K. B. In Situ Investigation of Chemomechanical Effects in Thiophosphate Solid Electrolytes. *Matter* **2020**, *3*, 2138.

(17) Dixit, M.; Verma, A.; Zaman, W.; Zhong, X.; Kenesei, P.; Park, J.-S.; Almer, J.; Mukherjee, P. P.; Hatzell, K. Synchrotron Imaging of Li Metal Anodes in Solid State Batteries Aided by Machine Learning. *ACS Appl. Energy Mater.* **2020**, *3*, 9534.

(18) Yui, Y.; Hayashi, M.; Nakamura, J. In situ microscopic observation of sodium deposition/dissolution on sodium electrode. *Sci. Rep.* **2016**, *6*, 22406.

(19) Hatzell, K. B.; Chen, X. C.; Cobb, C. L.; Dasgupta, N. P.; Dixit, M. B.; Marbella, L. E.; McDowell, M. T.; Mukherjee, P. P.; Verma, A.; Viswanathan, V.; et al. Challenges in lithium metal anodes for solid-state batteries. *ACS Energy Letters* **2020**, *5*, 922−934.

(20) Shen, F.; Dixit, M. B.; Xiao, X.; Hatzell, K. B. Effect of pore connectivity on Li dendrite propagation within LLZO electrolytes observed with synchrotron X-ray tomography. *ACS Energy Letters* **2018**, *3*, 1056−1061.

(21) Yu, Z.; Shang, S.-L.; Seo, J.-H.; Wang, D.; Luo, X.; Huang, Q.; Chen, S.; Lu, J.; Li, X.; Liu, Z.-K.; et al. Exceptionally High Ionic Conductivity in Na3P0. 62As0. 38S4 with Improved Moisture Stability for Solid-State Sodium-Ion Batteries. *Adv. Mater.* **2017**, *29*, 1605561.

(22) Zhou, D.; Liu, R.; Zhang, J.; Qi, X.; He, Y.-B.; Li, B.; Yang, Q.-H.; Hu, Y.-S.; Kang, F. In situ synthesis of hierarchical poly (ionic liquid)-based solid electrolytes for high-safety lithium-ion and sodium-ion batteries. *Nano Energy* **2017**, *33*, 45−54.

(23) Banerjee, A.; Park, K. H.; Heo, J. W.; Nam, Y. J.; Moon, C. K.; Oh, S. M.; Hong, S.-T.; Jung, Y. S. Na3SbS4: A Solution Processable Sodium Superionic Conductor for All-Solid-State Sodium-Ion Batteries. *Angew. Chem., Int. Ed.* **2016**, *55*, 9634−9638.

(24) de Klerk, N. J.; Wagemaker, M. Diffusion mechanism of the sodium-ion solid electrolyte Na3PS4 and potential improvements of halogen doping. *Chem. Mater.* **2016**, *28*, 3122−3130.

(25) Duchêne, L.; Kühnel, R.-S.; Stilp, E.; Cuervo Reyes, E.; Remhof, A.; Hagemann, H.; Battaglia, C. A stable 3 V all-solid-state sodium−ion battery based on a closo-borate electrolyte. *Energy Environ. Sci.* **2017**, *10*, 2609−2615.

(26) Gao, H.; Xin, S.; Xue, L.; Goodenough, J. B. Stabilizing a high-energy-density rechargeable sodium battery with a solid electrolyte. *Chem.* **2018**, *4*, 833−844.

(27) Lu, X.; Xia, G.; Lemmon, J. P.; Yang, Z. Advanced materials for sodium-beta alumina batteries: Status, challenges and perspectives. *J. Power Sources* **2010**, *195*, 2431−2442.

(28) Dixit, M. B.; Zaman, W.; Bootwala, Y.; Zheng, Y.; Hatzell, M. C.; Hatzell, K. B. Scalable manufacturing of hybrid solid electrolytes with interface control. *ACS Appl. Mater. Interfaces* **2019**, *11*, 45087−45097.

(29) Dixit, M. B.; Zaman, W.; Hortance, N.; Vujic, S.; Harkey, B.; Shen, F.; Tsai, W.-Y.; De Andrade, V.; Chen, X. C.; Balke, N.; et al. Nanoscale mapping of extrinsic interfaces in hybrid solid electrolytes. *Joule* **2020**, *4*, 207−221.

(30) Shen, F.; Dixit, M. B.; Zaman, W.; Hortance, N.; Rogers, B.; Hatzell, K. B. Composite electrode ink formulation for all solid-state batteries. *J. Electrochem. Soc.* **2019**, *166*, A3182.

(31) Wenzel, S.; Leichtweiss, T.; Weber, D. A.; Sann, J.; Zeier, W. G.; Janek, J. Interfacial reactivity benchmarking of the sodium ion conductors Na3PS4 and sodium $\beta$-alumina for protected sodium metal anodes and sodium all-solid-state batteries. *ACS Appl. Mater. Interfaces* **2016**, *8*, 28216−28224.

(32) Yu, Z.; Shang, S.-L.; Seo, J.-H.; Wang, D.; Luo, X.; Huang, Q.; Chen, S.; Lu, J.; Li, X.; Liu, Z.-K.; et al. Exceptionally High Ionic Conductivity in Na3P0. 62As0. 38S4 with Improved Moisture Stability for Solid-State Sodium-Ion Batteries. *Adv. Mater.* **2017**, *29*, 1605561.

(33) Hu, P.; Zhang, Y.; Chi, X.; Kumar Rao, K.; Hao, F.; Dong, H.; Guo, F.; Ren, Y.; Grabow, L. C.; Yao, Y. Stabilizing the Interface between Sodium Metal Anode and Sulfide-Based Solid-State Electrolyte with an Electron-Blocking Interlayer. *ACS Appl. Mater. Interfaces* **2019**, *11*, 9672−9678.

(34) Zaman, W.; Hortance, N.; Dixit, M. B.; De Andrade, V.; Hatzell, K. B. Visualizing percolation and ion transport in hybrid solid electrolytes for Li−metal batteries. *J. Mater. Chem. A* **2019**, *7*, 23914−23921.

(35) Riphaus, N.; Stiaszny, B.; Beyer, H.; Indris, S.; Gasteiger, H. A.; Sedlmaier, S. J. Understanding chemical stability issues between different solid electrolytes in all-solid-state batteries. *J. Electrochem. Soc.* **2019**, *166*, A975.

(36) Tian, Y.; Sun, Y.; Hannah, D. C.; Xiao, Y.; Liu, H.; Chapman, K. W.; Bo, S.-H.; Ceder, G. Reactivity-Guided Interface Design in Na Metal Solid-State Batteries. *Joule* **2019**, *3*, 1037−1050.

(37) Yubuchi, S.; Ito, A.; Masuzawa, N.; Sakuda, A.; Hayashi, A.; Tatsumisago, M. Aqueous solution synthesis for Na3SbS4-Na2WS4 superionic conductors. *J. Mater. Chem. A* **2020**, *8*, 1947.

(38) Liu, M.; Zhou, D.; He, Y.-B.; Fu, Y.; Qin, X.; Miao, C.; Du, H.; Li, B.; Yang, Q.- H.; Lin, Z.; et al. Novel gel polymer electrolyte for high-performance lithium−sulfur batteries. *Nano Energy* **2016**, *22*, 278−289.

(39) Chan, J. W.; Hoyle, C. E.; Lowe, A. B.; Bowman, M. Nucleophile-initiated thiol-michael reactions: effect of organocatalyst, thiol, and ene. *Macromolecules* **2010**, *43*, 6381−6388.

(40) Nair, D. P.; Podgorski, M.; Chatani, S.; Gong, T.; Xi, W.; Fenoli, C. R.; Bowman, C. N. The thiol-Michael addition click reaction: a powerful and widely used tool in materials chemistry. *Chem. Mater.* **2014**, *26*, 724−744.

(41) Nair, D. P.; Podgorski, M.; Chatani, S.; Gong, T.; Xi, W.; Fenoli, C. R.; Bowman, C. N. The thiol-Michael addition click reaction: a powerful and widely used tool in materials chemistry. *Chem. Mater.* **2014**, *26*, 724−744.

(42) Mather, B. D.; Viswanathan, K.; Miller, K. M.; Long, T. E. Michael addition reactions in macromolecular design for emerging technologies. *Prog. Polym. Sci.* **2006**, *31*, 487−531.

(43) Chan, J. W.; Hoyle, C. E.; Lowe, A. B.; Bowman, M. Nucleophile-initiated thiol-michael reactions: effect of organocatalyst, thiol, and ene. *Macromolecules* **2010**, *43*, 6381−6388.

(44) Lee, Y.-G.; Fujiki, S.; Jung, C.; Suzuki, N.; Yashiro, N.; Omoda, R.; Ko, D.-S.; Shiratsuchi, T.; Sugimoto, T.; Ryu, S.; et al. High-energy long-cycling all-solid-state lithium metal batteries enabled by silver−carbon composite anodes. *Nature Energy* **2020**, *5*, 299−308.

(45) Moon, C. K.; Lee, H.-J.; Park, K. H.; Kwak, H.; Heo, J. W.; Choi, K.; Yang, H.; Kim, M.-S.; Hong, S.-T.; Lee, J. H.; et al. Vacancy-driven Na+ superionic conduction in new Ca-doped Na3PS4 for all-solid-state Na-ion batteries. *ACS Energy Letters* **2018**, *3*, 2504−2512.

(46) Li, Y.; Wang, X.; Zhou, H.; Xing, X.; Banerjee, A.; Holoubek, J.; Liu, H.; Meng, Y. S.; Liu, P. Thin Solid Electrolyte Layers Enabled by Nanoscopic Polymer Binding. *ACS Energy Letters* **2020**, *5*, 955−961.

(47) Pang, Q.; Zhou, L.; Nazar, L. F. Elastic and Li-ion−percolating hybrid membrane stabilizes Li metal plating. *Proc. Natl. Acad. Sci. U. S. A.* **2018**, *115*, 12389−12394.

(48) Villaluenga, I.; Wujcik, K. H.; Tong, W.; Devaux, D.; Wong, D. H.; DeSimone, J. M.; Balsara, N. P. Compliant glass−polymer hybrid single ion-conducting electrolytes for lithium batteries. *Proc. Natl. Acad. Sci. U. S. A.* **2016**, *113*, 52−57.

(49) Whiteley, J. M.; Taynton, P.; Zhang, W.; Lee, S.-H. Ultra-thin solid-state Li-ion electrolyte membrane facilitated by a self-healing polymer matrix. *Adv. Mater.* **2015**, *27*, 6922−6927.

(50) Lu, Y.; Zhang, N.; Jiang, S.; Zhang, Y.; Zhou, M.; Tao, Z.; Archer, L. A.; Chen, J. High-capacity and ultrafast Na-ion storage of a self-supported 3D porous antimony persulfide−graphene foam architecture. *Nano Lett.* **2017**, *17*, 3668−3674.

(51) Ren, Y.; Jiang, H.; Zhao, T.; Zeng, L.; Xiong, C. Remedies of capacity fading in room-temperature sodium-sulfur batteries. *J. Power Sources* **2018**, *396*, 304−313.

(52) Xu, Z.-L.; Yoon, G.; Park, K.-Y.; Park, H.; Tamwattana, O.; Kim, S. J.; Seong, W. M.; Kang, K. Tailoring sodium intercalation in graphite for high energy and power sodium ion batteries. *Nat. Commun.* **2019**, *10*, 2598.

(53) Simon, F. J.; Hanauer, M.; Henss, A.; Richter, F. H.; Janek, J. Properties of the Interphase formed between Argyrodite-type Li6PS5Cl and Polymer-based PEO10: LiTFSI. *ACS Appl. Mater. Interfaces* **2019**, *11*, 42186−42196.

(54) Drewett, N. E.; Aldous, I. M.; Zou, J.; Hardwick, L. J. In situ Raman spectroscopic analysis of the lithiation and sodiation of antimony microparticles. *Electrochim. Acta* **2017**, *247*, 296−305.

(55) Chen, X.; Shen, X.; Li, B.; Peng, H.-J.; Cheng, X.-B.; Li, B.-Q.; Zhang, X.-Q.; Huang, J.-Q.; Zhang, Q. Ion−solvent complexes

promote gas evolution from electrolytes on a sodium metal anode. *Angew. Chem., Int. Ed.* **2018**, *57*, 734−737.

(56) Zhou, L.; Cao, Z.; Zhang, J.; Sun, Q.; Wu, Y.; Wahyudi, W.; Hwang, J.-Y.; Wang, L.; Cavallo, L.; Sun, Y.-K.; et al. Engineering Sodium-Ion Solvation Structure to Stabilize Sodium Anodes: Universal Strategy for Fast-Charging and Safer Sodium-Ion Batteries. *Nano Lett.* **2020**, *20*, 3247−3254.

(57) Wu, E. A.; Kompella, C. S.; Zhu, Z.; Lee, J. Z.; Lee, S. C.; Chu, I.-H.; Nguyen, H.; Ong, S. P.; Banerjee, A.; Meng, Y. S. New insights into the interphase between the Na metal anode and sulfide solid-state electrolytes: a joint experimental and computational study. *ACS Appl. Mater. Interfaces* **2018**, *10*, 10076−10086.

(58) Xu, X.; Li, Y.; Cheng, J.; Hou, G.; Nie, X.; Ai, Q.; Dai, L.; Feng, J.; Ci, L. Composite solid electrolyte of Na3PS4-PEO for all-solid-state SnS2/Na batteries with excellent interfacial compatibility between electrolyte and Na metal. *J. Energy Chem.* **2020**, *41*, 73−78.

(59) Tian, Y.; Shi, T.; Richards, W. D.; Li, J.; Kim, J. C.; Bo, S.-H.; Ceder, G. Compatibility issues between electrodes and electrolytes in solid-state batteries. *Energy Environ. Sci.* **2017**, *10*, 1150−1166.

(60) Ryu, H.; Kim, T.; Kim, K.; Ahn, J.-H.; Nam, T.; Wang, G.; Ahn, H.-J. Discharge reaction mechanism of room-temperature sodium−sulfur battery with tetra ethylene glycol dimethyl ether liquid electrolyte. *J. Power Sources* **2011**, *196*, 5186−5190.

(61) Zhou, L.; Cao, Z.; Zhang, J.; Sun, Q.; Wu, Y.; Wahyudi, W.; Hwang, J.-Y.; Wang, L.; Cavallo, L.; Sun, Y.-K.; et al. Engineering Sodium-Ion Solvation Structure to Stabilize Sodium Anodes: Universal Strategy for Fast-Charging and Safer Sodium-Ion Batteries. *Nano Lett.* **2020**, *20*, 3247−3254.

(62) Liu, H.; Pei, W.; Lai, W.-H.; Yan, Z.; Yang, H.; Lei, Y.; Wang, Y.-X.; Gu, Q.; Zhou, S.; Chou, S. Electrocatalysing S Cathodes via Multisulfiphilic Sites for Superior Room-Temperature Sodium-Sulfur Batteries. *ACS Nano* **2020**, *14*, 7259.

(63) Xu, X.; Zhou, D.; Qin, X.; Lin, K.; Kang, F.; Li, B.; Shanmukaraj, D.; Rojo, T.; Armand, M.; Wang, G. A room-temperature sodium−sulfur battery with high capacity and stable cycling performance. *Nat. Commun.* **2018**, *9*, 3870.